



Numerical Simulation of the Time-Dependent Mild-Slope Equation by the Generalized Finite Difference Method

TING ZHANG,¹ ZHEN-HUAN LIN,¹ CHUAN LIN,¹  LIN LIANG,¹ and CHIA-MING FAN²

Abstract—The time-dependent mild-slope equation (MSE) is a second-order hyperbolic equation, which is adopted to consider the irregularity of waves. For the difficulty of directly solving the partial derivative terms and the second-order time derivative term, a novel mesh-free numerical scheme, based on the generalized finite difference method (GFDM) and the Houbolt finite difference method (HFDM), is developed to promote the precision and efficiency of the solution to time-dependent MSE. Based on the local characteristics of the GFDM, as a new domain-type meshless method, the linear combinations of nearby function values can be straightforwardly and efficiently implemented to compute the partial derivative term. It is worth noting that the application of the HFDM, an unconditionally stable finite difference time marching scheme, to solve the second-order time derivative term is critical. The results obtained from four examples show that the propagation of waves can be successfully simulated by the proposed numerical scheme in complex seabed terrain. In addition, the energy conversion of waves in long-distance wave propagation can be accurately captured using fast Fourier transform (FFT) analysis, which investigates the energy conservation in wave shoaling problems.

Keywords: Time-dependent mild-slope equation, generalized finite difference method, meshless method, combined refraction and diffraction, Houbolt finite difference method.

1. Introduction

With the propagation of the wave train from a deep water to a shallow water region, various wave transformations including reflection, resonance, shoaling, combined refraction and diffraction, and wave breaking occur due to the changes in the seabed

topography. In the field of hydraulic and coastal engineering, as well as for the calculation of sediment transport, applying the above transformations during wave propagation is essential. Therefore, various forms of the mild-slope equation (MSE) have been widely applied to simulate the above combined effects. By supposing linear harmonic waves and overlooking rotation, bottom friction, and wave breaking, Berkhoff (1972) first derived the original MSE with the consideration of the combined influence of refraction, reflection, and diffraction for linear surface waves. Later, Smith and Sprinks (1975) formally deduced time-dependent MSE with asymptotic theory. For monochromatic waves with single frequency, it can be simplified to the original MSE, and they utilized it to study the problem of surface waves scattered by a conical island. Since three-dimensional problems are simplified to two-dimensional problems, combining the reliable description of refraction and diffraction, MSE has been universally used to handle coastal engineering problems.

As mentioned above, since the original MSE is derived from linear wave theory, it does not consider the effects of many additional physical phenomena such as friction, breaking, and wave nonlinearity on the wave transformations, which restricts its applicability. Therefore, many researchers have focused on modifying the original MSE, and a number of improvements have been suggested, such as introducing wave breaking (Battjes, 1978; Dally et al., 1985; Massel, 1992), frictional dissipation (Alvarez et al., 2017; Booij, 1981; Khellaf & Bouhadef, 2004), wave-current interaction (Kirby, 1984; Liu, 1983; Massel, 1992), and steep slope (James, 1986; Lee & Yoon, 2004; Zou et al., 2017) into the original MSE

¹ Department of Water Resources and Harbor Engineering, College of Civil Engineering, Fuzhou University, Fuzhou, China. E-mail: linchuan@fzu.edu.cn

² Department of Harbor and River Engineering and Computation and Simulation Center, National Taiwan Ocean University, Keelung 20224, Taiwan, China.

and extending it to a time-dependent equation (Beels et al., 2010a; Kim et al., 2006; Lee & Suh, 1998; Lin, 2004; Smith & Sprinks, 1975; Tsai et al., 2014). A mesh-free numerical method, the generalized finite difference method (GFDM) was first proposed to accurately and efficiently solve the original MSE in our previous study (Zhang et al., 2018). However, the original MSE can only be applied for the of steady-state wave predication, so the transient behavior of a wave, playing an essential role in real engineering, cannot be predicted. In this paper, it concentrates on proposing a newly-developed meshless numerical scheme to directly solve the time-dependent MSE. It is paramount to search a direct and effective numerical scheme for solving the time-dependent MSE, which is a hyperbolic partial differential equation combining with the second-order time derivative term. Therefore, in this paper, the GFDM and Houbolt finite difference method (HFDM) were respectively employed for spatial and temporal discretization to develop a novel numerical scheme which has the ability to deal with simulating transient wave movement by approximately estimating the propagation speed of wave energy.

The time-dependent MSE (Smith & Sprinks, 1975) has gained a good reputation for describing near coastal and offshore wave phenomena, especially combined diffraction and refraction, since it was developed more than four decades ago. Zhang et al. (1995) later derived a new form of time-dependent MSE for random waves using the Padé approximation and Kubo's time series concept, and their results proved that the new equation excels at describing both regular and random waves while neglecting bottom friction. A dispersive time-dependent MSE, which is composed of several depth-dependent functions in their most general form, was also developed by Beji and Nadaoka (1997). Lin (2004) established a numerical algorithm based on an explicit finite difference method (FDM) which has second-order temporal and spatial accuracy to model wave propagation, shoaling, together with refraction and diffraction, by solving the time-dependent MSE. Zhang et al. (2007) utilized the Euler predictor-corrector method and a three-point FDM with variable spatial steps to solve the time-dependent MSE considering bottom dissipation and nonlinearity. Tong

et al. (2010) presented an extension of the time-dependent MSE and solved it by adopting the alternating-direction implicit (ADI) method with a space-staggered grid to simulate wave propagation under the influence of rapidly varying depth in curvilinear coordinates. The time-dependent MSE has also been used to deal with realistic problems. Beels et al. (2010b) exploited the method to simulate the wake effects in the lee of a farm of Wave Dragon wave energy converters. Tsai et al. (2014) developed a set of second-order time-dependent MSEs using a perturbation method, and the equations were simplified to a nonlinear long-wave equation, a linear time-dependent MSE, and the traditional Boussinesq equation. In order to accurately generate regular waves and irregular long- and short-crested waves in any direction, the time-dependent MSE model was used to develop periodic lateral boundaries, i.e. MILDwave, by Vasarmidis et al. (2019). The studies mentioned above all have their own strengths and weaknesses in terms of applicability, accuracy, and computational cost, so a more reliable method is still needed to solve the time-dependent MSE.

To save the time of mesh generation and numerical integration, which are compulsory steps in traditional mesh-based methods and greatly decrease computational efficiency (especially in problems concerning high dimension and complex geometry) (Belytschko et al., 1996), meshless methods such as the element-free Galerkin method (EFGM) (Álvarez et al., 2018), the method of fundamental solutions (MFS) (Li et al., 2019a), the modified collocation Trefftz method (MCTM) (Fan et al., 2012, 2014), the meshless local Petrov-Galerkin method (MLPGM) (Li et al., 2019b), the local radial basis function (RBF) collocation method (LRBFCM) (Boudjaj et al., 2019), the local RBF-based differential quadrature method (LRBFDQM) (Wang et al., 2017), the smoothed-particle hydrodynamics (SPH) (Härdi et al., 2019), and the GFDM (Benito et al., 2001; Fan et al., 2015, 2019; Gavette et al., 2003; Li & Fan, 2017; Ureña et al., 2012, 2019, 2020; Zhang et al., 2016a, 2016b, 2018) have been proposed in recent decades.

Among the meshless methods mentioned above, as a domain-type meshless method, the numerical implementation of the GFDM only needs a group of

boundary nodes and a group of interior nodes. Then, the numerical predications can be easily acquired by enforcing the satisfaction of the governing equations at every interior node and the boundary conditions at every boundary node. Thus, this meshless method is easy to program, uncomplicated, and efficient. At the same time, the application of localization helps the GFDM avoid the problems of ill-conditioned matrices. An explicit formula for the GFDM was developed by Benito et al. (2001), and used four mathematical examples to examine many critical factors for the numerical accuracy. Subsequently, Gavette et al. (2003) improved the GFDM, whose superiority over the element-free Galerkin method (EFGM) was already demonstrated. Ureña et al. applied an extension of the GFDM to solve high-order partial differential equations (PDE) (Ureña et al., 2012), and the nonlinear parabolic and hyperbolic PDE (Ureña et al., 2019, 2020) obtained the explicit solution. In the past few years, the GFDM has been employed to solve various mathematical questions and engineering applications including two-dimensional inverse Cauchy problems (Fan et al., 2015), the two-dimensional liquid sloshing flows problem (Zhang et al., 2016a), the propagation of nonlinear waves (Zhang et al., 2016b), the shallow water equation (Li & Fan, 2017), the mild-slope equation (Zhang et al., 2018), and wave-current interactions (Fan et al., 2019).

In this paper, the GFDM and the HFDM were respectively adopted for spatial and temporal discretization of the time-dependent MSE (Houbolt, 1950; Lin et al., 2014; Najarzadeh et al., 2019; Soroushian & Farjoodi, 2008; Young et al., 2008) to study wave transformations, including shoaling, reflection, and combined refraction and diffraction. As the spatial derivatives of every computational node can be easily obtained by the function values of their own nearby nodes, this shows that the GFDM has the flexibility of spatial discretization and simplicity of the implementation process. From the above description, it is worth noting that the proposed numerical method really eliminates mesh generation and numerical quadrature, which can deal with the difficulty of solving the spatial partial derivative terms. After the discretization by the HFDM, every node marches the time step with the second-order

time derivative term, and the free surface displacement will change at each time step simultaneously. Next, the GFDM is applied for solving the time-dependent MSE at the present time step. It is worth mentioning that the speed of propagation and wave dispersion can be captured well. Specifically, the numerical scheme presented herein is fit to simulate the wave propagation and deformation for a larger and more complicated computational domain due to the simple numerical procedures and flexible distribution of nodes. The numerical results obtained imply that it is successful for the employed numerical scheme to simulate the time-dependent MSE.

The remainder of the paper is organized as follows. The governing equations and the boundary condition are presented in Sect. 2. The proposed numerical procedures combining the GFDM and HFDM are described in Sect. 3. In Sect. 4, four examples are presented to validate the capability of the presented meshless numerical method in solving the time-dependent MSE, and the numerical results are compared with other numerical results.

2. Governing Equation and Boundary Conditions

2.1. Governing Equations

The MSE has been widely applied for the description of wave propagation containing refraction and diffraction over a slowly varying topography. Thus, wave propagation in a numerical model over different bottoms and $h(x, y)$ denote still water depth, which is considered in this study to simulate this phenomenon. As depicted in Fig. 1, the Cartesian coordinate system, (x, y) , is laid on the free surface.

The governing equation herein adopts the time-dependent MSE proposed by Smith and Sprinks (1975). The time-dependent MSE incorporating the second-order time derivative term can be expressed by:

$$\begin{aligned} \frac{\partial^2 \eta}{\partial t^2} - \frac{\partial(cc_g)}{\partial x} \frac{\partial \eta}{\partial x} - \frac{\partial(cc_g)}{\partial y} \frac{\partial \eta}{\partial y} - cc_g \left(\frac{\partial^2 \eta}{\partial x^2} + \frac{\partial^2 \eta}{\partial y^2} \right) \\ + (\omega^2 - k^2 cc_g) \eta \\ = 0, \end{aligned} \quad (1)$$

where η denotes the free surface displacement, and t

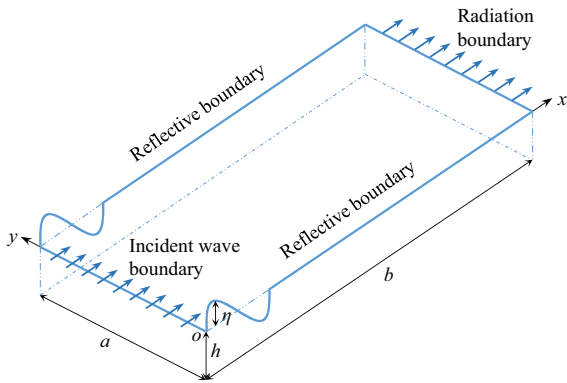


Figure 1

Schematic diagram of computational domain and boundary conditions

represents time, c stands for the phase velocity and c_g stands for the group velocity, which are respectively calculated as follows:

$$c = \frac{\omega}{k}, \quad c_g = \frac{d\omega}{dk} = \frac{c}{2} \left(1 + \frac{2kh}{\sinh 2kh} \right). \quad (2)$$

Based on the dispersion relation, the relationship between the local wave number k and angular frequency ω can be described as follows:

$$\omega^2 = gk \tanh(kh). \quad (3)$$

2.2. Boundary Conditions

To accurately simulate wave motion in a numerical model, suitable boundary conditions are of great importance. Thus, three types of boundary conditions described below are considered herein. As depicted in Fig. 1, a wave with wave height H_0 propagates into the computational domain from the left boundary, and this wave is specified as the incident boundary condition:

$$\eta(t) = \frac{H_0}{2} \sin(\omega t). \quad (4)$$

The right boundary displayed in Fig. 1 specifies the radiation boundary condition, which signifies that the waves can leave the domain freely. A second-order radiation boundary condition is adopted in this study (Engquist & Majda, 1977), which is defined by:

$$\frac{\partial^2 \eta}{\partial t^2} + c \frac{\partial^2 \eta}{\partial n \partial t} - \frac{c^2}{2} \frac{\partial^2 \eta}{\partial s^2} = 0, \quad (5)$$

in which n and s denote the normal outward and tangential directions at the right radiation boundary, respectively.

Lateral boundaries are solid, which implies that the waves are fully reflected. The expression of this boundary condition is also given by:

$$\frac{\partial \eta}{\partial n} = 0. \quad (6)$$

3. Numerical Methods

The GFDM and the HFDM are employed herein for spatial and temporal discretization, respectively. HFDM is mainly used to manage the time derivative terms in the governing equations and radiation boundary conditions, while GFDM is employed to process the MSE at the current time step depending on the updated value of the free surface displacement. All calculation nodes in the computational domain are fixed, whether an interior node or boundary node, so once the nodes are distributed, the weighting coefficient of each node can be determined. The concrete analysis of the GFDM and the HFDM are presented in the following sections.

3.1. Houbolt Finite Difference Method (HFDM)

As mentioned above, the time-dependent MSE is a second-order hyperbolic equation with transient terms. HFDM is a three-step implicit and strictly stable time-integration method. The time operators can be approximately computed by the values of the four levels from $t^{n-2} = (n-2)\Delta t$ to $t^{n+1} = (n+1)\Delta t$ when t^{n+1} using the Lagrange interpolation. Thus, the first- and second-order time operators can be expressed by:

$$\left(\frac{\partial \eta}{\partial t} \right)^{n+1} \approx \frac{1}{6\Delta t} (11\eta^{n+1} - 18\eta^n + 9\eta^{n-1} - 2\eta^{n-2}), \quad (7)$$

$$\left(\frac{\partial^2 \eta}{\partial t^2} \right)^{n+1} \approx \frac{1}{\Delta t^2} (2\eta^{n+1} - 5\eta^n + 4\eta^{n-1} - \eta^{n-2}), \quad (8)$$

in which Δt denotes the time increment, and η^n represents the free surface displacement at time n , i.e. $\eta^n(x) = \eta(x, t^n)$.

Since four time levels are considered in both of the above formulas, the setup problem has to be managed. Thus, the Euler scheme is adopted herein to handle the problem as follows:

$$\begin{cases} \eta^{n-1} = \eta_I - \Delta t \cdot \eta_{II} \\ \eta^{n-2} = \eta_I - 2\Delta t \cdot \eta_{II} \end{cases}, \quad n \leq 2, \quad (9)$$

in which the subscripts I and II indicate the first- and second-order partial derivatives in the initial time with the following expressions:

$$\begin{cases} \eta(\vec{x}, t)|_{t=0} = \eta_I(\vec{x}) \\ \frac{\partial \eta(\vec{x}, t)}{\partial t}|_{t=0} = \eta_{II}(\vec{x}), \end{cases} \quad (10)$$

The computation starts from the $n+1$ th time step, and the water is initially still in the computational domain. Therefore, the wave elevation at the three previous time steps are set as $\eta^n(x, y) = 0$, $\eta^{n-1}(x, y) = 0$, and $\eta^{n-2}(x, y) = 0$.

3.2. Generalized Finite Difference Method (GFDM)

In this section, based on the moving least squares (MLS) method, the numerical implementation of GFDM for the spatial discretization in solving two-dimensional wave propagation under different boundary conditions problems is briefly introduced.

First, two sets of nodes are generated in the computational domain, namely the scattered interior nodes and the boundary nodes, and the distribution can be arbitrary or uniform. Then, a small computational subdomain, defined as a cluster, is circled out by the n_s closest nodes around a given i th node. Various options for the shapes of the cluster have been presented elsewhere (Benito et al., 2001). In this paper, a circular cluster, which is widely applied, is chosen for simplicity. Theoretically, the greater the number of nodes selected in the cluster, the more accurate the results obtained; nonetheless, n_s should be optimized according to the accuracy preferred and the computational cost required. According to

previous studies (Fan et al., 2015; Ureña et al., 2020; Zhang et al., 2016a, b), for practical computations solved with the GFDM, satisfactory precision can be achieved when n_s is larger than 10. Consequently, n_s is set at 10 for all the examples presented in this work.

After forming the cluster of the i th node, a new function, $B(\eta)$, can be defined by Taylor series expansion using the spatial positions and physical quantities of the n_s closest points (Benito et al., 2001; Fan et al., 2015; Gavette et al., 2003; Ureña et al., 2012, 2019, 2020; Zhang et al., 2016a, b) as follows:

$$B(\eta) = \sum_{j=1}^{n_s} \left\{ \left(\eta_i - \eta_j^i + \mathbf{c}_{ij} \mathbf{D}_u \right) w_{ij} \right\}^2, \quad (11)$$

where $\mathbf{D}_u = \left(\frac{\partial \eta}{\partial x} \Big|_i, \frac{\partial \eta}{\partial y} \Big|_i, \frac{\partial^2 \eta}{\partial x^2} \Big|_i, \frac{\partial^2 \eta}{\partial y^2} \Big|_i, \frac{\partial^2 \eta}{\partial x \partial y} \Big|_i \right)^T$ denotes the vector of unknown derivatives at the i th node, and $\mathbf{c}_{ij} = \left(h_{ij}, k_{ij}, \frac{h_{ij}^2}{2}, \frac{k_{ij}^2}{2}, h_{ij}k_{ij} \right)$ signifies the coefficients corresponding to the unknown derivatives. j is the local index in the star, and $\{x_j^i, y_j^i\}_{j=1}^{n_s}$ represents the coordinates of the n_s nodes. $h_{ij} = x_i - x_j^i$ and $k_{ij} = y_i - y_j^i$ represent the distances between the i th node and the j th node along the x and y directions, respectively. $w_{ij} = w(h_{ij}, k_{ij})$ is the value of the positive symmetrical weighting function at (x_j^i, y_j^i) . Among the proposed weighting functions, including quartic spline, cubic spline, and potential function (Benito et al., 2001; Gavette et al., 2003; Ureña et al., 2012, 2019), the quartic spline was adopted in this study.

Next, based on Eq. (11), a linear system can be generated by minimizing function $B(\eta)$ with respect to $\mathbf{D}_u = \left\{ \frac{\partial \eta}{\partial x} \Big|_i, \frac{\partial \eta}{\partial y} \Big|_i, \frac{\partial^2 \eta}{\partial x^2} \Big|_i, \frac{\partial^2 \eta}{\partial y^2} \Big|_i, \frac{\partial^2 \eta}{\partial x \partial y} \Big|_i \right\}^T$. The linear system can be expressed by:

$$\mathbf{A} \mathbf{D}_u = \mathbf{b}, \quad (12)$$

where

$$\mathbf{A} = \sum_{j=1}^{n_s} w_{ij}^2 \mathbf{c}_{ij}^T \mathbf{c}_{ij}, \quad (13)$$

$$\mathbf{b} = \sum_{j=1}^{n_s} w_{ij}^2 \left(-\eta_i + \eta_j^i \right) \mathbf{c}_{ij}^T. \quad (14)$$

Consequently, the derivatives vector, \mathbf{D}_u , is defined as follows:

$$\begin{aligned} \mathbf{D}_u &= \mathbf{A}^{-1} \mathbf{b} = -\mathbf{A}^{-1} \sum_{j=1}^{n_s} w_{ij}^2 \eta_i \mathbf{c}_{ij}^T + \mathbf{A}^{-1} \sum_{j=1}^{n_s} w_{ij}^2 \eta_j^i \mathbf{c}_{ij}^T \\ &= \mathbf{W}_0^i \eta_i + \sum_{j=1}^{n_s} \mathbf{W}_j^i \eta_j^i, \end{aligned} \quad (15)$$

in which

$$\mathbf{W}_0^i = -\mathbf{A}^{-1} \sum_{j=1}^{n_s} w_{ij}^2 \mathbf{c}_{ij}^T, \quad (16)$$

$$\mathbf{W}_j^i = \mathbf{A}^{-1} w_{ij}^2 \mathbf{c}_{ij}^T, \quad (17)$$

where \mathbf{W}_0^i and \mathbf{W}_j^i represent the relevant weighting coefficients in the star of the i th point and can be computed numerically. Then, the spatial derivative of each node can be computed by the linear combination of the product of the nearby function value and the corresponding weighting coefficient by performing the above process.

Finally, a sparse system of linear algebraic equations, which is used to acquire the ultimate numerical solutions, can be generated by enforcing the satisfaction of the governing equations at all interior nodes and the boundary conditions at all boundary nodes. Meanwhile, it can be found that although the following four numerical examples use uniform discrete points, as a meshless method, the numerical method presented indeed eliminates mesh generation and numerical quadrature by constructing the approximation entirely in terms of points. Since the above derivational procedures, i.e. exploiting the GFDM to tackle the second-order PDE, have been clearly discussed in previous studies (Benito et al., 2001; Fan et al., 2015; Gavette et al., 2003; Ureña et al., 2012, 2019, 2020; Zhang et al., 2016a, b), readers are encouraged to refer to these published works for further details.

3.3. Solving Time-Dependent MSE with GFDM and HFDM

After temporal discretization by the HFDM, the governing equation, Eq. (1), and the radiation boundary condition, Eq. (5), can be respectively rewritten as follows:

$$\begin{aligned} &\{2 + \Delta t^2 (\sigma^2 - k^2 c c_g)\} \eta^{n+1} \\ &- \Delta t^2 \left\{ \frac{\partial (c c_g)}{\partial x} \frac{\partial \eta^{n+1}}{\partial x} + \frac{\partial (c c_g)}{\partial y} \frac{\partial \eta^{n+1}}{\partial y} \right\} \\ &- \Delta t^2 c c_g \left(\frac{\partial^2 \eta^{n+1}}{\partial x^2} + \frac{\partial^2 \eta^{n+1}}{\partial y^2} \right) = 5 \eta^n - 4 \eta^{n-1} + \eta^{n-2}, \end{aligned} \quad (18)$$

$$\begin{aligned} &2 \eta^{n+1} + \frac{11 c \Delta t}{6} \frac{\partial \eta^{n+1}}{\partial x} - \frac{c^2 \Delta t^2}{2} \frac{\partial^2 \eta^{n+1}}{\partial y^2} \\ &= 5 \eta^n - 4 \eta^{n-1} + \eta^{n-2} \\ &+ \frac{c \Delta t}{6} \left(18 \frac{\partial \eta^n}{\partial x} - 9 \frac{\partial \eta^{n-1}}{\partial x} + 2 \frac{\partial \eta^{n-2}}{\partial x} \right). \end{aligned} \quad (19)$$

The procedure for analyzing the time-dependent MSE at the present time level by adopting the GFDM for the spatial discretization is then presented as follows (see Fig. 1). In fact, n_i nodes represent interior nodes in the computational domain, and n_{b1} , n_{b2} , n_{b3} , and n_{b4} nodes represent boundary nodes distributed at the incoming wave boundary, radiation boundary, and two side-wall boundaries, respectively. The partial derivatives of every node/point can then be easily expressed by following procedures defined in Eqs. (11)–(17).

Enforcing every interior node satisfies the governing equation, Eq. (18), which can generate a set of n_i linear equations, as given with the following expression:

$$\begin{aligned}
 & \{2 + \Delta t^2 (\sigma^2 - k^2 cc_g)\} \eta_i^{n+1} \\
 & - \Delta t^2 \left(E_0^{x,i} (cc_g)_i + \sum_{j=1}^{n_s} E_j^{x,i} (cc_g)_j \right) \\
 & \left(E_0^{x,i} \eta_i^{n+1} + \sum_{j=1}^{n_s} E_j^{x,i} \eta_j^{n+1,i} \right) \\
 & - \Delta t^2 \left(E_0^{y,i} (cc_g)_i + \sum_{j=1}^{n_s} E_j^{y,i} (cc_g)_j \right) \\
 & \left(E_0^{y,i} \eta_i^{n+1} + \sum_{j=1}^{n_s} E_j^{y,i} \eta_j^{n+1,i} \right) \\
 & - \Delta t^2 cc_g \left(E_0^{xx,i} \eta_i^{n+1} + \sum_{j=1}^{n_s} E_j^{xx,i} \eta_j^{n+1,i} \right. \\
 & \left. + E_0^{yy,i} \eta_i^{n+1} + \sum_{j=1}^{n_s} E_j^{yy,i} \eta_j^{n+1,i} \right) \\
 & = 5\eta_i^n - 4\eta_i^{n-1} + \eta_i^{n-2} \quad i = 1, 2, 3, \dots, n_i.
 \end{aligned} \tag{20}$$

In addition, by enforcing the fulfillment of the boundary conditions at every boundary node, another system of linear algebraic equations can be generated as follows:

$$\begin{aligned}
 \eta_i^{n+1} &= \frac{H_0}{2} \sin(\omega t^{n+1}) \\
 i &= n_i + 1, n_i + 2, n_i + 3, \dots, n_i + n_{b1},
 \end{aligned} \tag{21}$$

$$\begin{aligned}
 -\frac{\partial \eta^{n+1}}{\partial y} \Big|_i &= -E_0^{y,i} \eta_i^{n+1} - \sum_{j=1}^{n_s} E_j^{y,i} \eta_j^{n+1,i} = 0 \\
 i &= n_i + n_{b1} + 1, n_i + n_{b1} \\
 &+ 2, n_i + n_{b1} + 3, \dots, n_i + n_{b1} + n_{b2},
 \end{aligned} \tag{22}$$

$$\begin{aligned}
 2\eta^{n+1} &+ \frac{11c\Delta t}{6} \left(E_0^{x,i} \eta_i^{n+1} + \sum_{j=1}^{n_s} E_j^{x,j} \eta_j^{n+1,i} \right) \\
 &- \frac{c^2 \Delta t^2}{2} \left(E_0^{yy,i} \eta_i^{n+1} + \sum_{j=1}^{n_s} E_j^{yy,j} \eta_j^{n+1,i} \right) \\
 &= 5\eta^n - 4\eta^{n-1} + \eta^{n-2} + 3c\Delta t \left(E_0^{x,i} \eta_i^n + \sum_{j=1}^{n_s} E_j^{x,j} \eta_j^{n,i} \right) \\
 &- \frac{3c\Delta t}{2} \left(E_0^{x,i} \eta_i^{n-1} + \sum_{j=1}^{n_s} E_j^{x,j} \eta_j^{n-1,i} \right) \\
 &+ \frac{c\Delta t}{3} \left(E_0^{x,i} \eta_i^{n-2} + \sum_{j=1}^{n_s} E_j^{x,j} \eta_j^{n-2,i} \right) \\
 i &= n_i + b_1 + b_2 + 1, n_i + b_1 + b_2 + 2, n_i \\
 &+ b_1 + b_2 + 3, \dots, n_i + b_1 + b_2 + b_3,
 \end{aligned} \tag{23}$$

$$\begin{aligned}
 \frac{\partial \eta^{n+1}}{\partial y} \Big|_i &= E_0^{y,i} \eta_i^{n+1} + \sum_{j=1}^{n_s} E_j^{y,i} \eta_j^{n+1,i} = 0 \\
 i &= n_i + n_{b1} + n_{b2} + n_{b3} + 1, n_i + n_{b1} \\
 &+ n_{b2} + n_{b3} + 2, \dots, N.
 \end{aligned} \tag{24}$$

where N denotes the total number of nodes.

Thereafter, the above equations Eqs. (20)–(24) are combined to generate a new system of linear algebraic equations as follows:

$$[\mathbf{E}]_{N \times N} \{ \eta^{n+1} \}_{N \times 1} = \{ \mathbf{g} \}_{N \times 1}, \tag{25}$$

where $[\mathbf{E}]$ denotes a sparse coefficient matrix, on account of the sparsity of which only 10 corresponding nodes within the star are considered for every computed node. $\{ \mathbf{g} \}$ is composed of the homogeneous terms of the governing equation and the boundary data.

The numerical results of η at time $(n+1)$ th can be easily obtained by calculating Eq. (25), both at all interior and boundary points, and the values of every point at the next time are solved at the previous time step. The simulation then continues until the wave motion in the whole computational domain reaches a stable state.

According to the above description, the time-dependent MSE, which contains spatial partial derivative terms and second-order time derivative terms, can be directly and efficiently solved by the proposed numerical method. Hence, the partial derivatives of the governing equation and boundary conditions can be discretized by the GFDM to effectively simplify the numerical procedures. In the following section, four quintessential numerical examples of the combined diffraction and refraction problem are adopted to demonstrate that the presented simulation model can successfully simulate wave propagation.

4. Numerical Results and Comparisons

Four numerical examples of the combined refraction and diffraction are used to substantiate the

stability, accuracy, and simplicity of the numerical algorithm presented in the preceding section in solving the time-dependent MSE. The problems of two-dimensional waves propagating at invariable and variable water depth are simulated in the first two examples (Lin, 2004). In the third example, a numerical simulation of wave propagation over a submerged elliptic shoal at a slope, in which both wave refraction and diffraction are obvious, will be performed (Berkhoff et al., 1982; Cerrato et al., 2017; Hamidi et al., 2012; Karperaki et al., 2019; Panchang et al., 1991; Tang et al., 2004). Finally, as the fourth example, the experiment of Chawla and Kirby is adopted for simulation considering wave refraction and diffraction over submerged shoals (Chawla & Kirby, 1996; Chen & Kirby, 2000; Song et al., 2007). The results obtained by the proposed numerical scheme will be compared with other numerical predictions and available experimental data to validate the applicability.

4.1. Propagation of Short and Long Waves at Constant Water Depth

In order to examine the validity of the proposed method, a problem when a one-dimensional linear wave propagates over invariant water depth is considered as the first example. The first target is to test the minimum number of nodes needed in one wavelength to reach the appropriate precision of the simulation predictions; this minimum number of points will subsequently serve as the basis for more complex two-dimensional computations. The second goal is to examine the effectiveness of the radiation and wall boundary conditions, as defined in Eqs. (6) and (7), in absorbing and reflecting waves. Finally, it is significant for real-time wave forecasting to demonstrate the ability of the proposed numerical model to tackle transient problems.

As is generally known, group velocities and phase velocities are two critical parameters in wave propagation, and the group velocities are always lower than the phase velocities in deep water. Due to the wave energy transmission with the speed of group

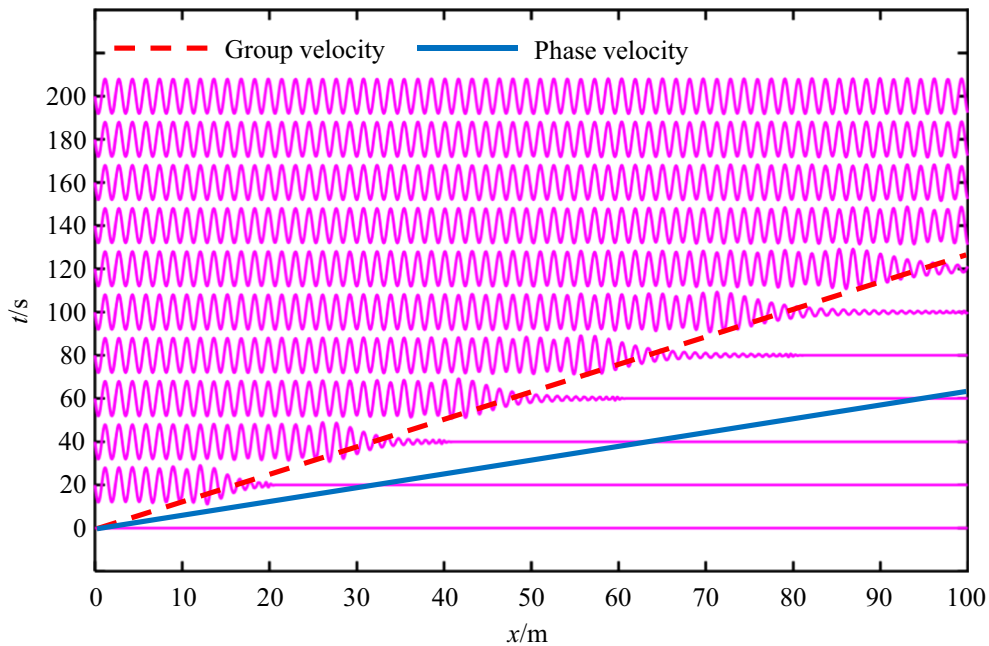


Figure 2
Propagation of short waves ($kh = 4.03$) into still water

velocity, derived from the linear wave theory, when a wave train propagates into still deep water, wave crests vanish at the location of $x = c_g t$ (where x is the wave propagation direction and c_g represents group velocity), which proceeds at a speed lower than the phase velocity. This effect is indicated in Fig. 2.

In this example, both short and long waves are evaluated. In the first test, a short wave train propagates into a numerical flume with 100 m length and 1.5 m width, where the water depth is kept constant and $h = 1$ m. The wave period and height are $T = 1$ s and $H_0 = 0.01$ m, respectively. The radiation boundary condition defined by Eq. (6) is set at $x = 100$ m. In this test, the phase velocity is $c = 1.559$ m s⁻¹, the group velocity is $c_g = 0.783$ m s⁻¹, corresponding to $kh = 4.03$, the distance between the nodes is $\Delta x = 0.1$ m, and the time increment is denote $\Delta t = 0.04$ s; according to this condition, about 16 points can describe one wavelength. The profiles of free surface along the central horizontal axis at different specific times are delineated in Fig. 2. As shown in Fig. 2, the wave

speed, preceding in the wave train, is nearly equal to c_g , i.e. group velocity. Due to the wave dispersion, it can be clearly noted that some leakage of wave energy appears when the wave speed is close to the group velocity. Furthermore, a well-established wave train (e.g. $t = 200$ s) is formed when the leading wave front leaves the computational domain freely through the radiation boundary. Obviously, the above phenomenon verifies the validity of the boundary condition defined in Eq. (2). In addition, the numerical results indicate that 16 nodes in one wavelength are sufficient to achieve reasonable accuracy.

In the second example, wave period $T = 20$ s is chosen as a long wave for simulation at the same water depth and compared with the short wave. The phase velocity and group velocity are respectively 3.127 and 3.116 m s⁻¹, with $kh = 0.101$; the parameters of Δx and Δt are 1.0 m and 0.1 s, respectively. According to the numerical results demonstrated in Fig. 3, the thick solid line and the thick dashed line nearly coincide. This implies that the wave phase velocity is almost equal to the group velocity. Owing

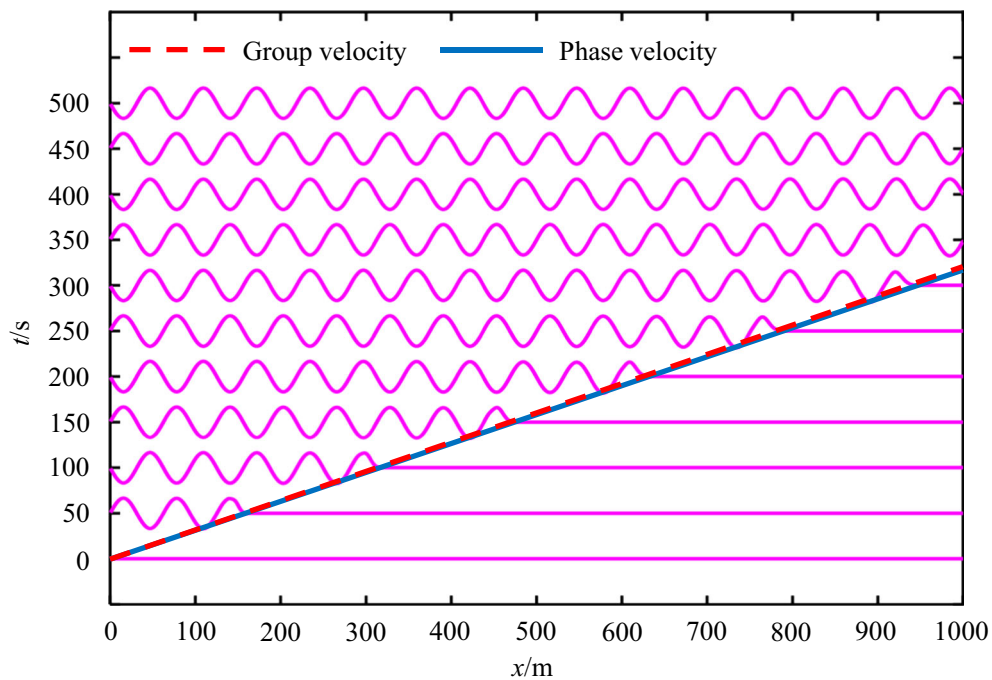


Figure 3
Propagation of long waves ($kh = 0.101$) into still water

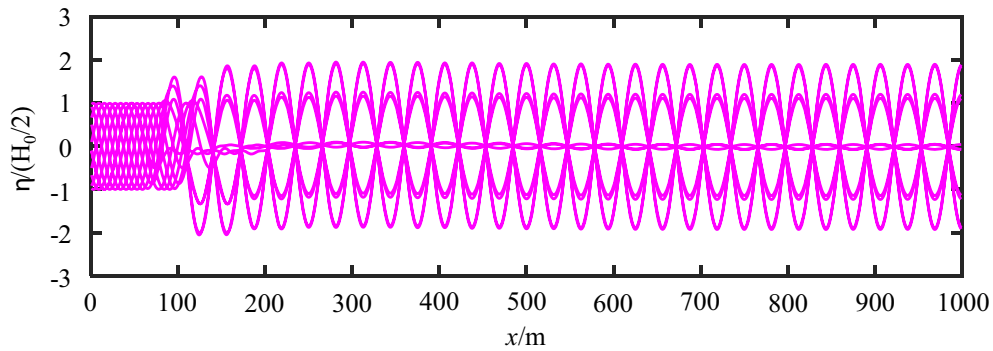


Figure 4
Standing waves when right boundary changes from radiation boundary to solid wall

to the varied insignificant wave dispersion, unlike the shortwave, the wave peak does not disappear in front of the longwave propagation. Additionally, in the propagation of long waves, the characteristic of the wave rough propagation at group velocity in the propagation is accurately simulated. Similarly, a well-established wave train is formed (see $t = 500$ s), which verifies the validity of the boundary condition defined in Eq. (5).

To further analyze the solid boundary condition as described in Eq. (6), the numerical results of changing the radiation boundary condition to the solid boundary condition are depicted in Fig. 4 with the simulation time t from 600 to 620 s. A perfect standing wave is formed in front of the solid wall, which proves the validity of the solid boundary condition.

4.2. Wave Shoaling from Deep to Shallow Water

Based on the wave propagation in the two previous examples, this case examines a one-dimensional long-distance wave propagation with a shoaling problem to indicate the ability of the proposed numerical model to simulate the conservation of wave energy in this process. When waves propagate from deep to shallow water, wave energy density and wave height (indirectly proportional to the square root of wave energy density) change with the velocity of the local group. Dean and Dalrymple

(1991) derived the shoaling formula from the conservation of energy flux as follows:

$$c_g E = \text{constant} \Rightarrow c_g H^2 = \text{constant}, \quad (26)$$

Herein, an idealized case of a linear wave train propagating across a continental shelf from deep water to shallow water was selected to simulate the effect of wave shoaling. As presented in Fig. 5, the whole computational domain is 200 km in length and 1.5 km in width, in which the deep water at a depth of 3000 m is connected at a mild slope of 2% to the shallow water at a depth of 40 m. The period and the wave height of the incident wave are 60 s and 0.01 m, respectively. The parameter of $(kh)_d$ is equal to 3.365 in the deep water and $(kh)_s$ is 0.213 in the shallow water. Therefore, the incident wave is classified as a short wave in the deep ocean but as a long wave in the shallow water region.

The energy flux and wave height along the centerline are depicted in Fig. 5. When the waves propagate from deep water to intermediate-depth water, the wave height gradually decreases with the increase in group velocity. Then, the wave height rises sharply when the waves propagate to a shallow water area. Moreover, the line of energy flux along the centerline is roughly horizontal from deep to shallow water. These findings are in good agreement with the physical meaning described by the shoaling formula, i.e. Eq. (26). This implies that the proposed meshless numerical scheme can ensure energy conservation in long-distance wave propagation. In

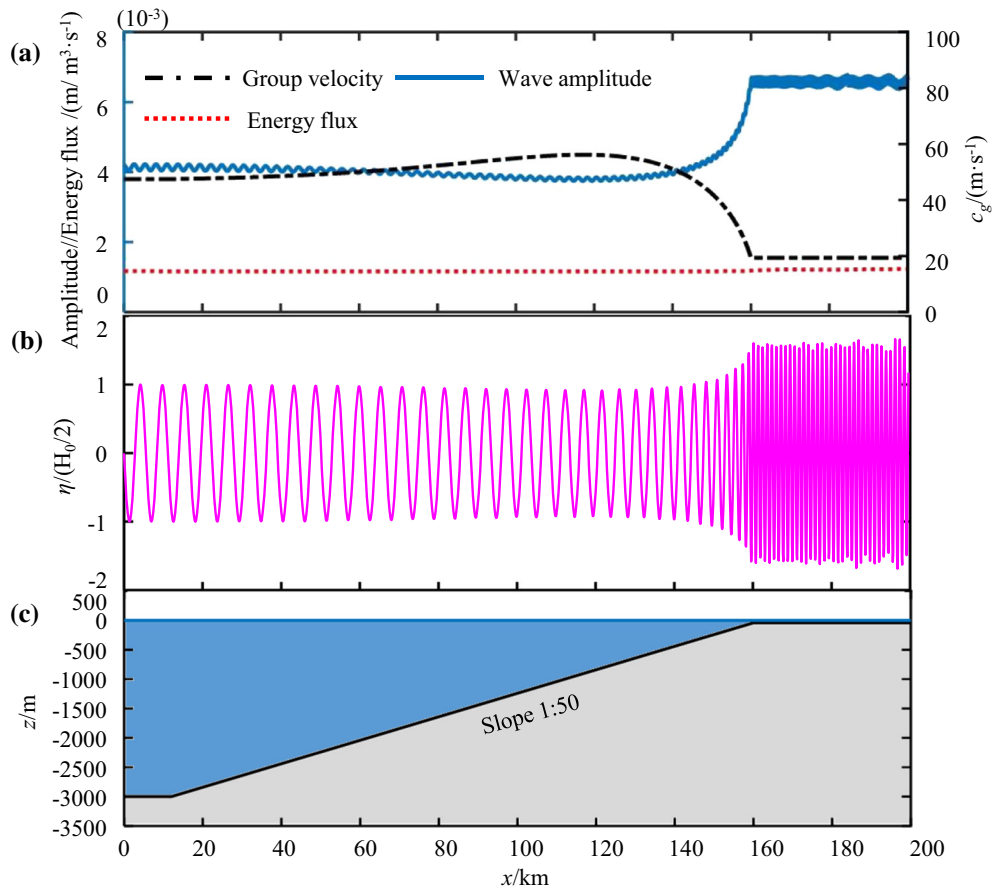


Figure 5

Wave shoaling when propagating from deep water into shallow water: **a** profiles of group velocity (c_g), wave amplitude and energy flux, **b** profile of wave height, and **c** schematic diagram of topography for wave shoal model

addition, the wave amplitude of first harmonic based on fast Fourier transform (FFT) analysis is also illustrated in Fig. 5. It can be noted that the wave amplitude of first harmonics increases with propagation to an area of shallower water, which indicates that a significant amount of energy of first harmonic increases due to the wave shoaling effect. Hence, the satisfactory practicability and stability of using the GFDM to tackle the time-dependent MSE are confirmed.

4.3. Wave Refraction and Diffraction over Submerged Elliptic Shoal at Slope

In this example, considering refraction and diffraction, waves propagating over a submerged elliptic shoal located on a slope were analyzed. The physical model device presented by Berkhoff et al. (1982), as a classic example, is adopted by many researchers (Berkhoff et al., 1982; Cerrato et al., 2017; Hamidi et al., 2012; Karperaki et al., 2019; Panchang et al., 1991; Tang et al., 2004) to verify their numerical models. This case was described by the original MSE in our previous work (Zhang et al., 2018). Therefore, this classic case of simulated coupled refraction and diffraction is modeled using

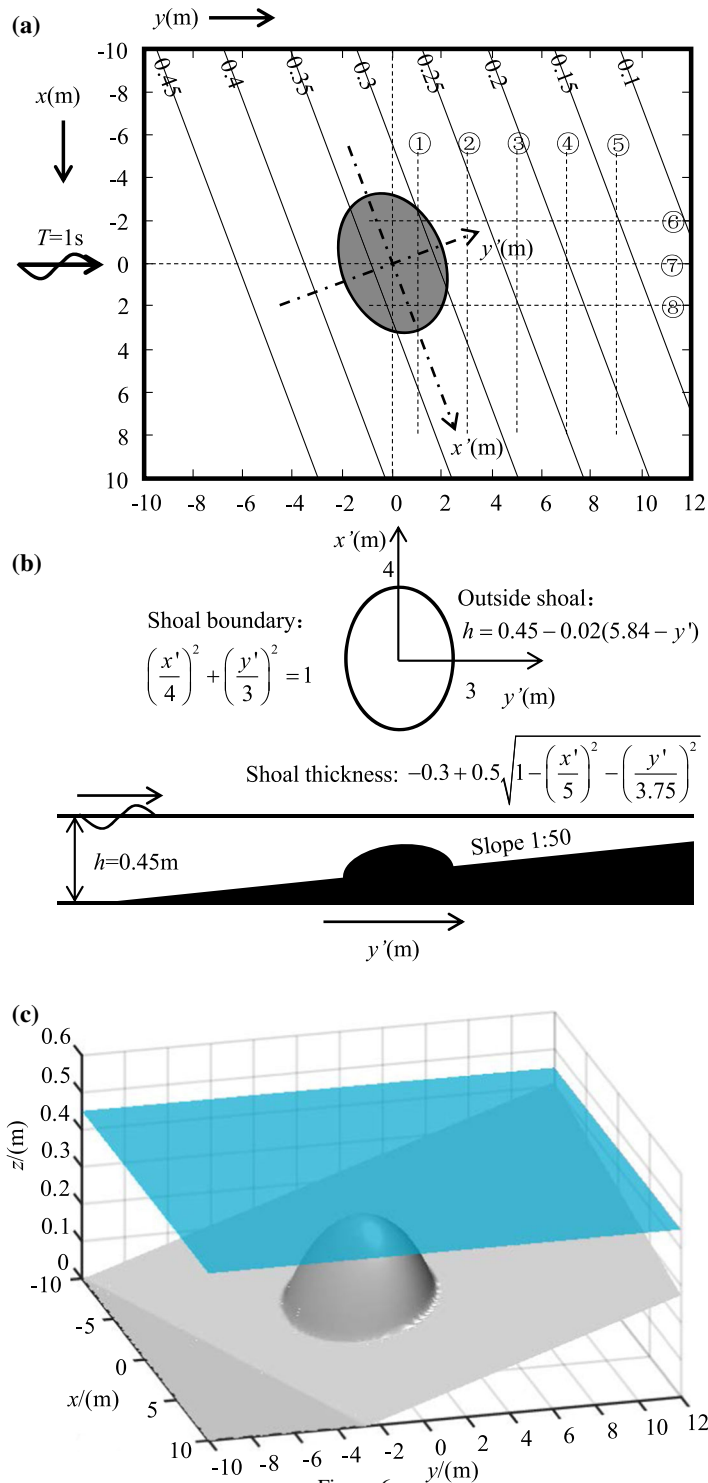


Figure 6

Schematic view of a experimental model, b topography, and c 3D presentation of elliptical shoal (Berkhoff et al., 1982)

the GFDM to tackle the time-dependent MSE to verify the feasibility of the numerical model presented herein.

As displayed in Fig. 6, an elliptic shoal is mounted on a sloping beach with a slope of 2%, and the coordinate origin is set in the center of the elliptic shoal. The incident wave, whose height and period are 0.0464 m and 1 s, respectively, enters the computational domain from the left boundary at $y = -10$ m and propagates across to the right absorption boundary at $y = -12$ m. Two reflection boundary conditions are respectively set at $x = -10$ m and $x = 10$ m.

Referring to Fig. 6, the slope oriented coordinates (x', y') are applied, which correspond to the computational coordinates (x, y) as follows:

$$\begin{aligned} x' &= (x - x_0) \cos 20^\circ + (y - y_0) \sin 20^\circ \\ y' &= (y - y_0) \cos 20^\circ - (x - x_0) \sin 20^\circ, \end{aligned} \quad (27)$$

where $(x_0, y_0) = (0, 0)$ represents the center of the shore, so the position of the shoal can be expressed by:

$$\left(\frac{x'}{4}\right)^2 + \left(\frac{y'}{3}\right)^2 < 1. \quad (28)$$

The water depth out of range of the shoal is given by:

$$\begin{aligned} h_s &= 0.45 - 0.02(5.84 + y') \quad y' \geq -5.84 \text{ m} \\ h_s &= 0.45 \quad y' < -5.84 \text{ m}. \end{aligned} \quad (29)$$

The water depth above the shoal is also defined by:

$$h = h_s + 0.3 - 0.5 \sqrt{1 - \left(\frac{x'}{5}\right)^2 - \left(\frac{y'}{3.75}\right)^2}. \quad (30)$$

In the numerical procedure, the parameters of Δx and Δt are respectively set at 0.05 m and 0.01 s, and the total calculation time is $t = 60 T$. It is known that the unknown physical quantity in the governing equation is the free surface displacement (η). In addition, the relative wave height (H/H_0) is presented here to compare our results with the other different schemes. It was computed by adopting the free surface displacement within 20 periods after the wave propagation achieved the steady state in the

computational domain. In other words, the maximum free surface displacement at each node in the wave period range of $35 T$ to $55 T$ is regarded as the amplitude at the node, and the wave height (H) is then computed.

The comparison between the GFDM and other previous results of relative wave heights at the eight different transections are presented in Fig. 6 and demonstrated in Fig. 7, including the experimental data and numerical results by the finite element method (Berkhoff et al., 1982), the solutions of the original MSE obtained by the FDM (Panchang et al., 1991), and the localized differential quadrature method (LDQM) (Hamidi et al., 2012), as well as the nonlinear findings of the model of the original MSE in our previous study (Zhang et al., 2018). It is clearly observed that a satisfactory estimation is achieved by comparison with other numerical results. Moreover, the results of the proposed method were very close to the results from the FDM (blue line) and the LDQM (red line). Unfortunately, some differences can be observed between the present model and the experimental data at certain positions in some sections, as well as between the other numerical models and the experimental data, especially from $y = 6$ m to $y = 10$ m in Sect. 8. They are mainly due to the influence of the linear MSE model, which has also been mentioned in previous studies. For example, Kirby and Dalrymple (1984) obtained better results by replacing the linear dispersion relation with a nonlinear dispersion relationship. Based on this nonlinear model, Hamidi et al. (2012) also obtained more accurate results which were nearly identical to the experimental data. Furthermore, the same conclusion was reached by using the nonlinear model of the original MSE (Zhang et al., 2018), as shown in Fig. 7. However, no research has introduced the nonlinear effects into the time-dependent MSE, so future work should investigate the nonlinear model of the time-dependent MSE.

4.4. Asymmetric Model of Submerged Circular Shoal

In the last example, an asymmetric model is analyzed, and the computational domain is demonstrated in Fig. 8. There is a submerged circular shoal in the rectangular computational domain with a

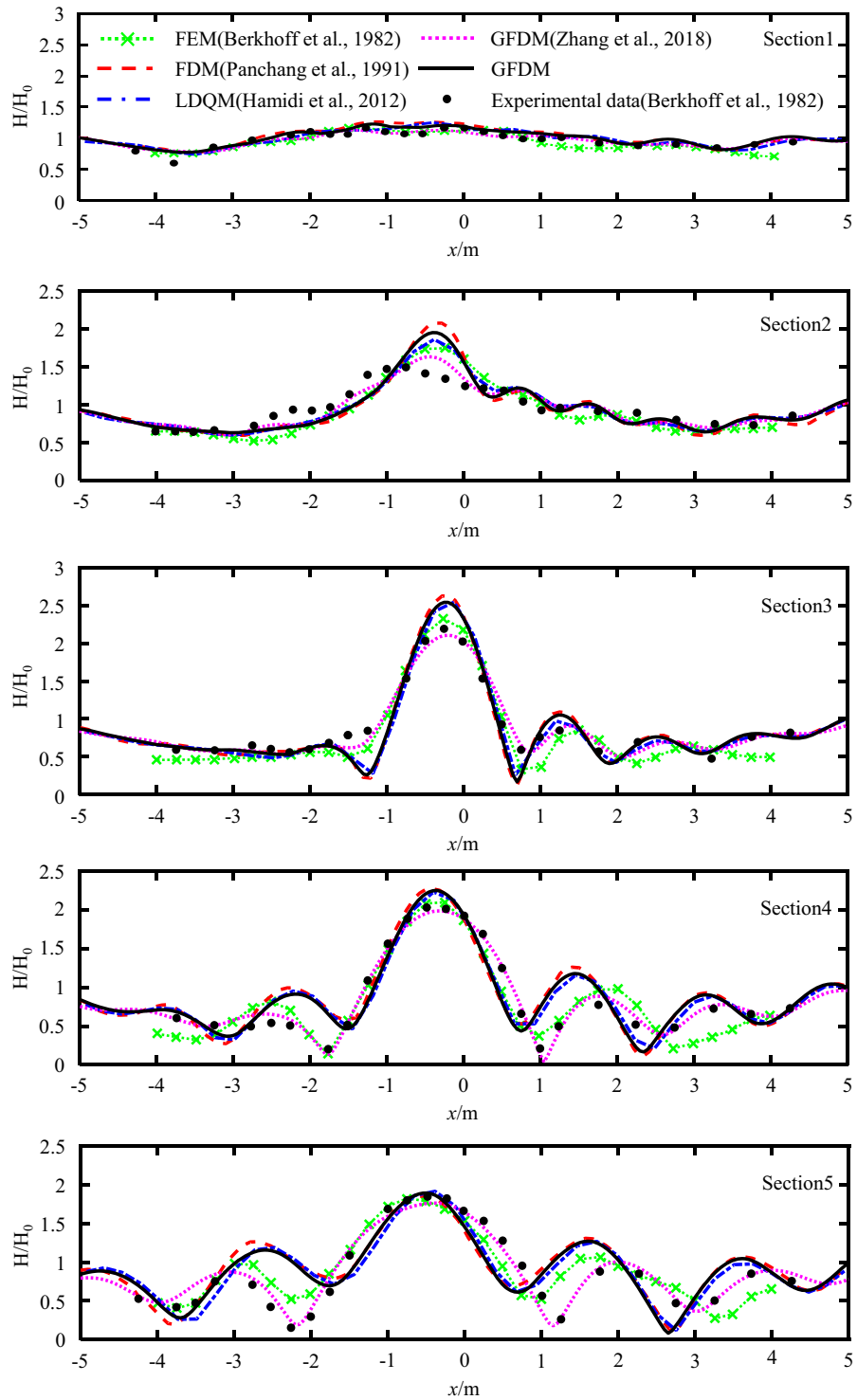


Figure 7
GFDM results of relative wave heights in comparison with experimental data and other numerical results

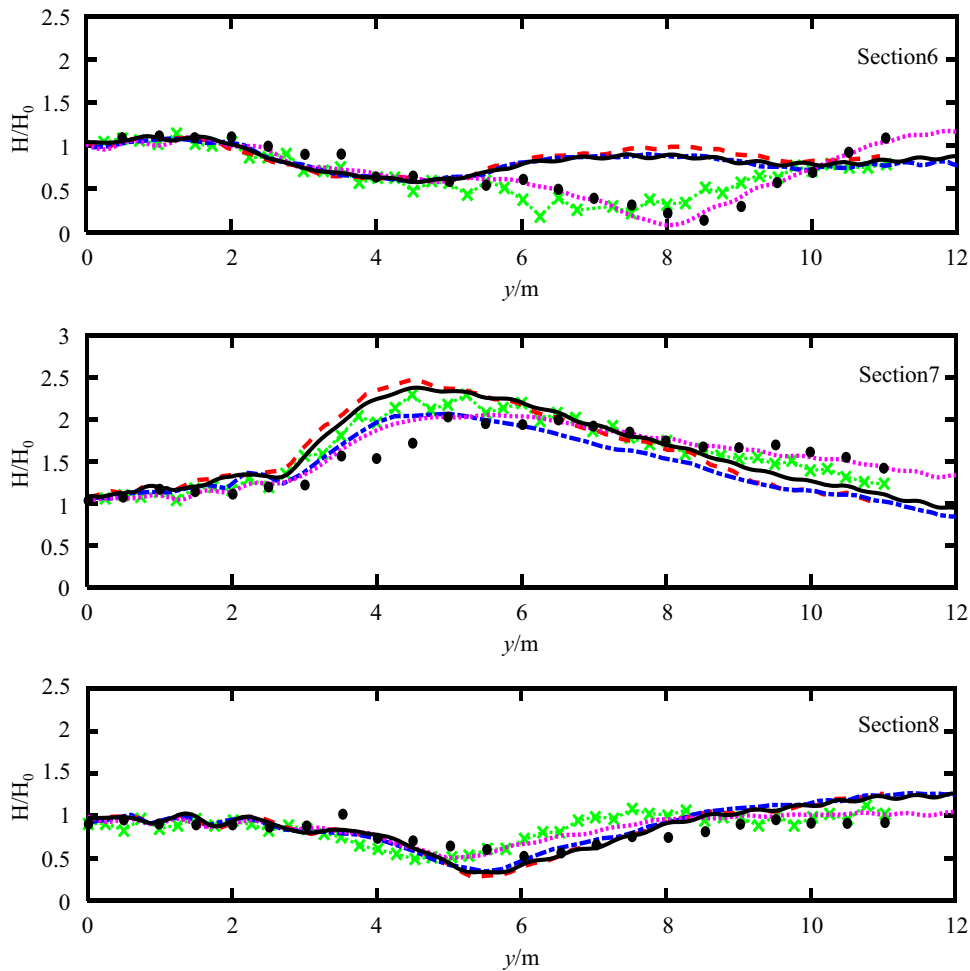


Figure 7 continued

radius of 2.57 m. The length and width of the rectangular domain are 20 m and 18.2 m, respectively. The incident waves with wave height $H_0 = 1.18$ cm and wave period $T = 1$ s propagate over the computational domain from the left open boundary to the right absorption boundary, and the reflection boundary conditions are imposed along the other two lateral closed boundaries. The position of the shoal is set as:

$$(x - 5)^2 + (y - 8.98)^2 = 2.57^2. \quad (31)$$

The water depth out of range of the shoal is 0.45 m, and the water depth above the shoal is described as follows:

$$h(x, y) = 9.18 - \sqrt{82.81 - (x - 5)^2 - (y - 8.98)^2}. \quad (32)$$

This model was proposed by Chawla and Kirby (1996), and a range of experiments including regular waves, irregular waves, breaking waves, and non-breaking waves were carried out. Later, Chen and Kirby (2000) utilized it to verify the Boussinesq model, and Song et al. (2007) used the time-dependent MSE to simulate the model. However, in the previous studies, the wave height results are all presented using the form of the root mean square. In the accessible references, except for section A–A as shown in Fig. 8, no work gives the location of other sections. Accordingly, considering that the previous

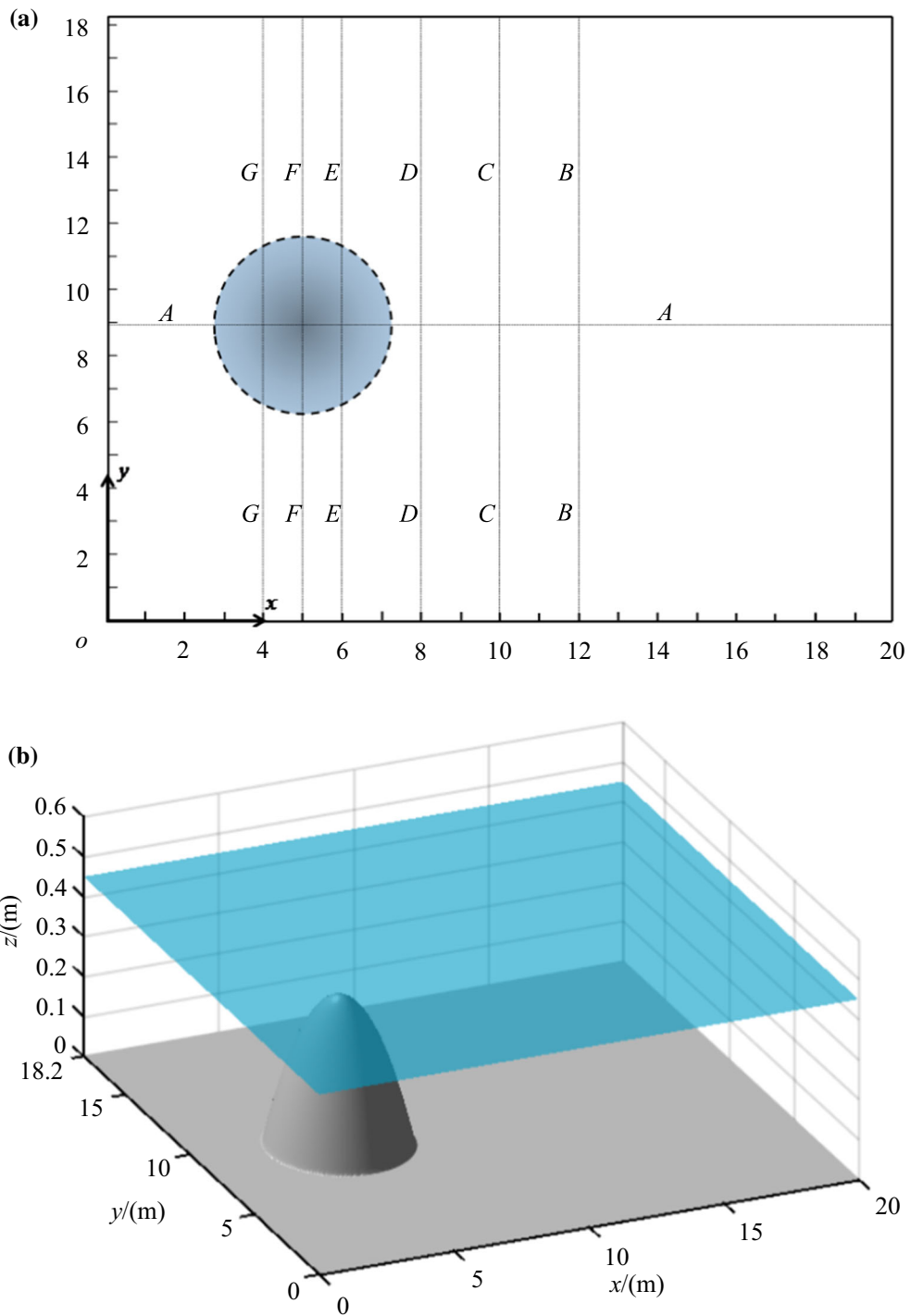


Figure 8
Schematic view of **a** experimental model and **b** 3D presentation of circular shoal

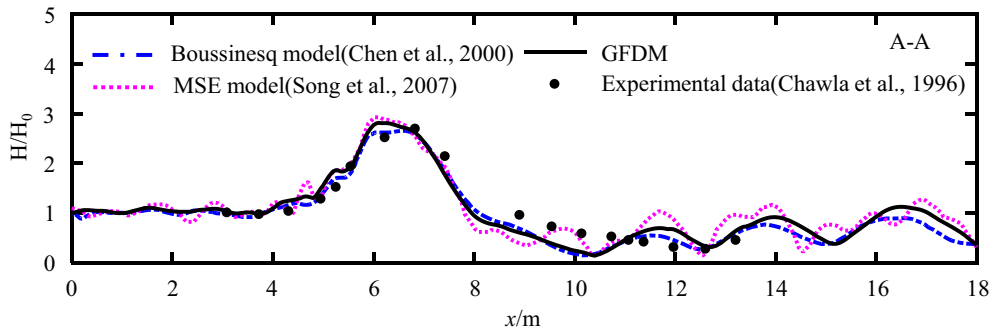


Figure 9

GFDM results of relative wave heights in comparison with experimental data and other numerical results in A–A section

examples proved the feasibility of using the GFDM to solve the MSE, the comparison at section A–A, among the GFDM results, other numerical predictions, and experimental data, is used to confirm that the proposed numerical scheme is practical and accurate. Then, the other sections are defined, as illustrated in Fig. 8, and the predictions are provided in the form of the relative wave height, which will provide a reference for future research on this model. Additionally, three different space intervals (Δx), of 0.2, 0.1, and 0.05 m and three time increments (Δt) of 0.01, 0.025, and 0.05 s are selected to evaluate the convergence of the simulation model.

The simulation runs until the wave propagation achieves a steady state, about 50 s. As in the previous example, for the sake of comparison between our results and the previous findings, which are presented in the form of the relative wave height (H/H_0), the maximum free surface displacement at each point in the wave period range of $35 T$ to $50 T$, during which the wave propagation reaches the steady state in the computational domain, is regarded as the amplitude at the point. Then, the wave height, H , is calculated.

The comparison of steady-state results at the A–A section, among the GFDM, other numerical models and experimental data, is shown in Fig. 9. Our results are in excellent agreement with the other solutions. The results of using different space intervals (Δx) and time increments (Δt) at seven sections are also depicted in Figs. 10 and 11, respectively.

In Fig. 10, the time increment is set at 0.025 s. It can be observed in the A–A section that with a

decrease in Δx , the simulation results gradually approach the experimental data. When $\Delta x = 0.1$ m, the relative wave height tends to converge, and a space interval of 0.05 m produces converging results which are almost the same as the experimental data. At the same time, there is similar convergence in other sections, so it is concluded that the converging numerical result is obtained when the space interval is equal to 0.1 m. In Fig. 11, the space interval is set at 0.05 m. Similarly, the simulation results gradually approach the experimental data with a decrease in the time increment (Δt) in the A–A section. When $\Delta t = 0.025$ s, the relative wave height tends to converge, and a time increment of 0.01 s results in converging predictions which are almost in agreement with the experimental data. The similar convergence also remains in other sections. Thus, it is concluded that the converging numerical result is achieved when the time increment is equal to 0.025 s.

According to the steady-state profile of the three-dimensional free surface illustrated in Fig. 12, the distribution of waves is generally symmetrical. Nevertheless, since the position of the submerged shoal is slightly biased towards the negative direction of the y -axis, the distribution of the waves seems slightly asymmetrical. Figure 13 shows the three-dimensional free surface profiles at $t = 5$ s, $t = 10$ s, $t = 15$ s, and $t = 20$ s. It can be seen in Fig. 13a that the wave propagates from one side of the computational domain and just reaches the front of the shoal at $t = 5$ s. The wave then washes over the shoal and deformation appears due to the influence of the shoal

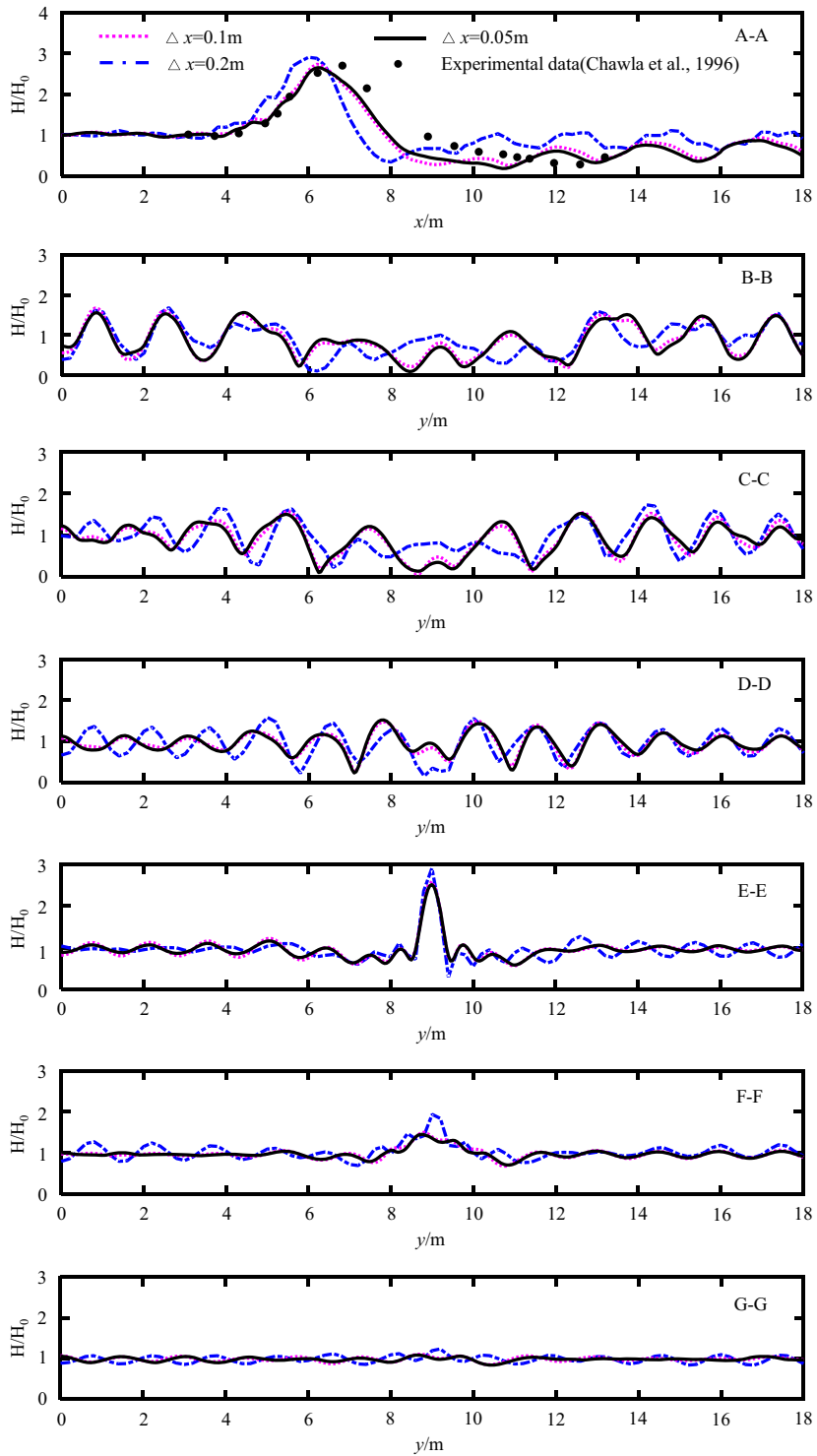


Figure 10
 Profiles of relative wave height at different space intervals (the time increment $\Delta t = 0.025$ s)

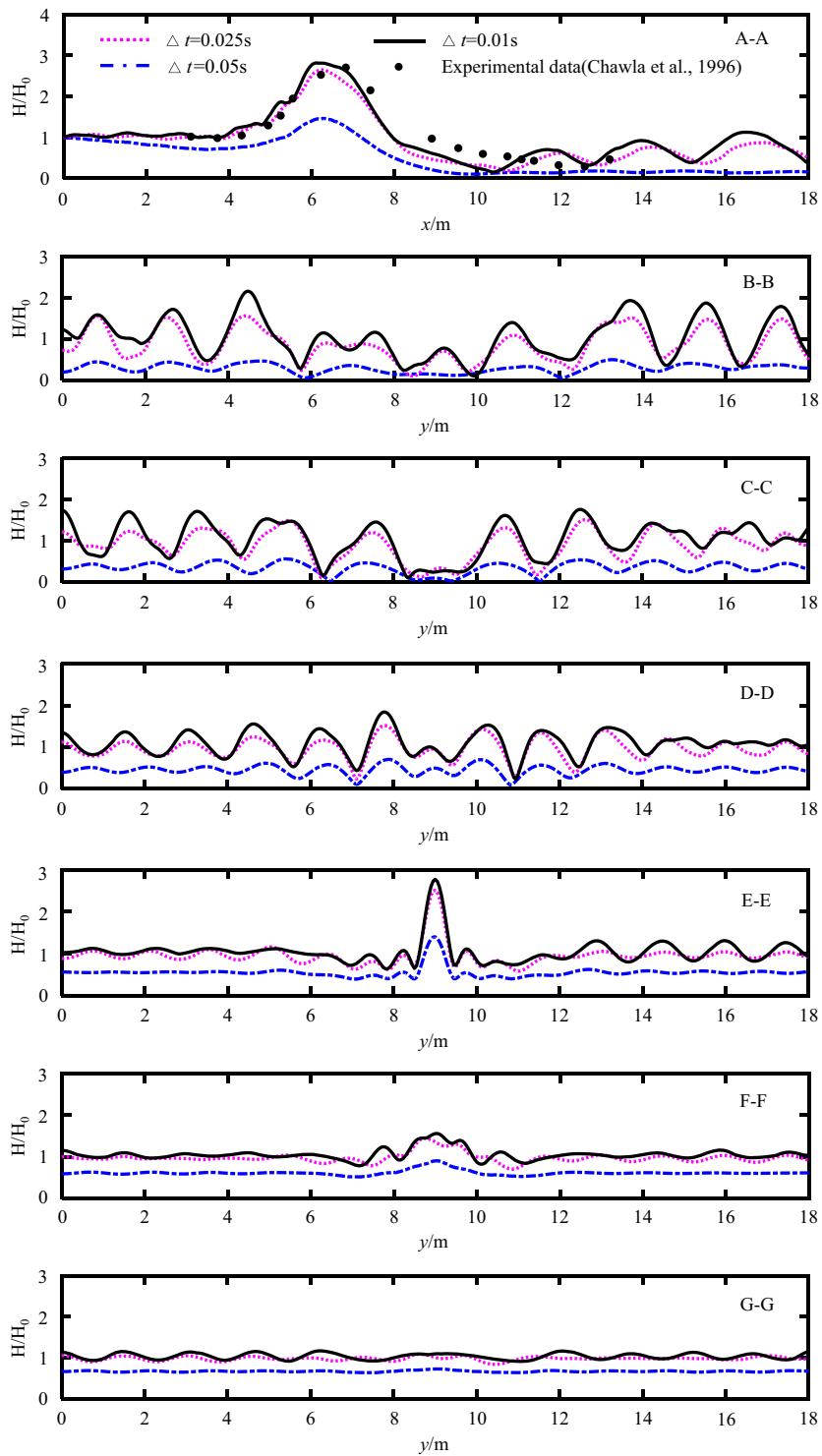


Figure 11
 Profiles of relative wave height at different time increments (the space interval $\Delta x = 0.025$ s)

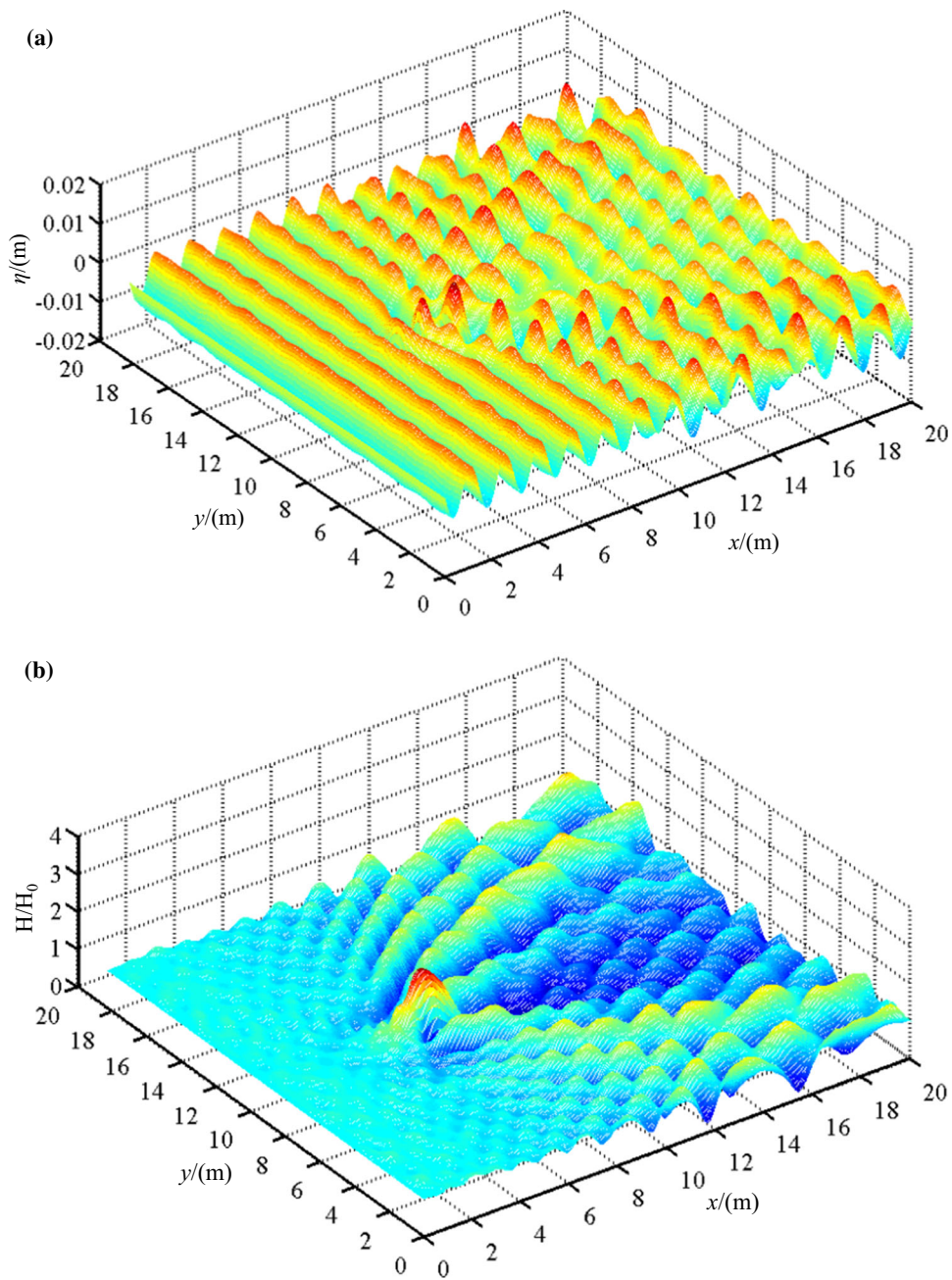


Figure 12

3D presentation of GFDM results of circular shoal model: **a** free surface elevation and **b** relative wave height

in Fig. 13b, c. Then, Fig. 13d shows that the wave passes the shoal and will eventually develop into a steady-state motion at $t = 20$ s. It can be clearly observed that the wave deformation occurs because of the influence of the submerged circular shoal,

which demonstrated the applicability of the proposed meshless model to deal with transient problems.

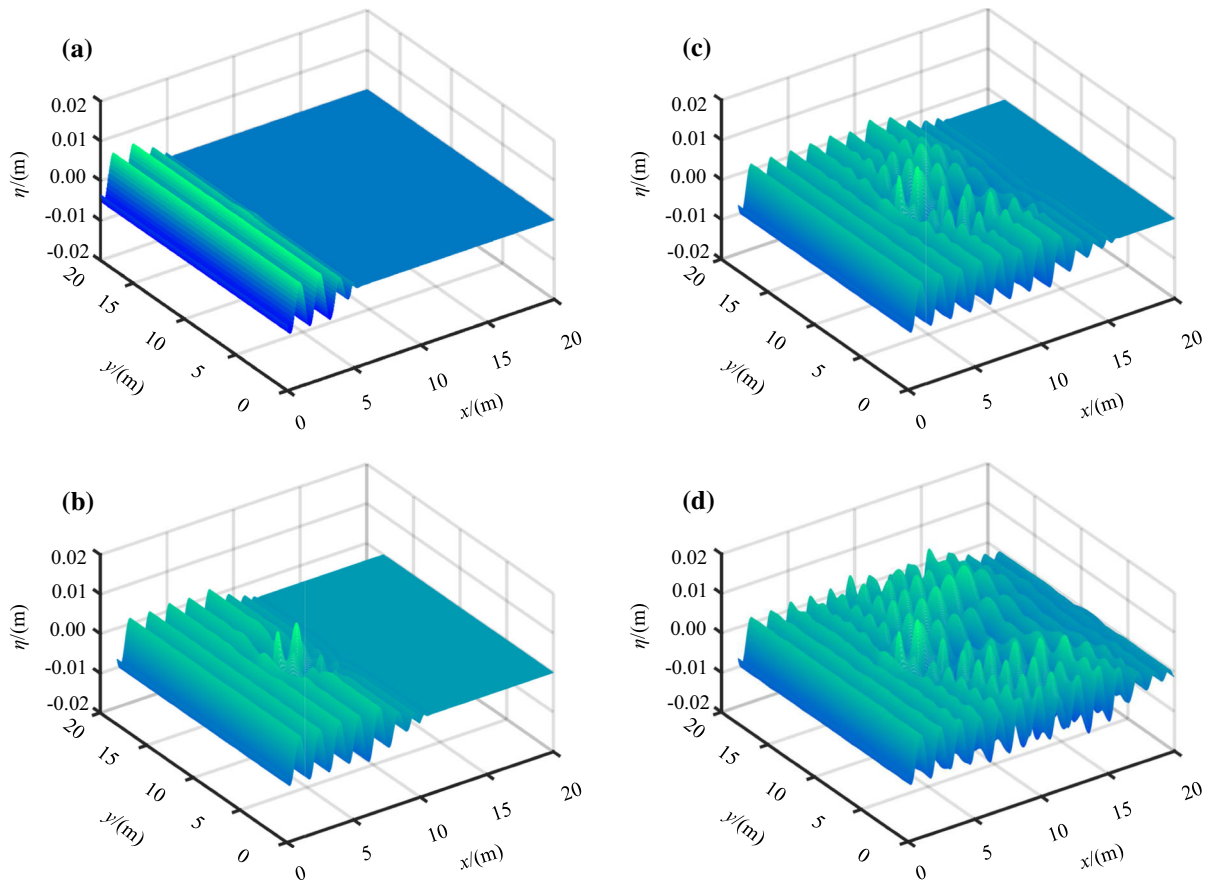


Figure 13
Three-dimensional profiles of free surfaces at **a** $t = 5$ s, **b** $t = 10$ s, **c** $t = 15$ s, **d** $t = 20$ s

5. Discussion and Conclusions

In this work, a novel meshless numerical scheme based on the GFDM and the HFDM was first developed to solve the time-dependent MSE. Since marching the time step with the second-order time derivative term is arduous, there are few numerical methods that have been developed to solve it directly. Coupled with the HFDM, an unconditionally stable finite difference time marching scheme for solving the second-order time derivative term, the GFDM has been applied to the time-dependent MSE for solving the problem of waves. Based on the GFDM, the time-dependent MSE at each point can be simply, straightforwardly, and efficiently converted into the linear combinations of the product of nearby function values and the corresponding weight

coefficients. Therefore, the numerical procedure of the GFDM and the HFDM in solving the time-dependent MSE can be easily implemented by addressing a sparse system of linear algebraic equations, which can achieve sufficient accuracy.

Four numerical examples were provided, and the comparison among the numerical results, the available experimental results, and other simulation results were also provided to validate the applicability of the proposed meshless numerical scheme. In the first two numerical examples, the problems of one-dimensional wave propagation at a constant and variable water depth were studied, and it was demonstrated that the proposed method can accurately capture the transient feature of wave advancement into still water and simulate transient wave motion accurately by correctly predicting the speed of wave energy

propagation. In addition, the energy transformation of waves in long-distance wave propagation is accurately captured based on FFT analysis, in which the wave amplitude and wave height change with the velocity of the local group. This indicates that the proposed numerical scheme can ensure the conservation of wave energy in the wave shoaling problem. In the last two examples, the ability of the proposed method to simulate wave reflection and diffraction processes was also proved by studying wave propagation in complex bottom topography. It can be observed that the proposed numerical model can accurately capture the wave profiles since satisfying results are obtained by comparing with experimental and other simulation results. In addition, six other sections were defined in our last example and different space intervals and time increments were considered to examine the stability and convergence of the presented numerical simulation model. Finally, the proposed model proves to be an excellent tool to predict the transient behavior of waves. In general, it is concluded that the proposed numerical model can efficiently and accurately deal with the time-dependent MSE and has good flexibility to deal with complex wave propagation problems.

Although satisfactory results were obtained in these examples, and the practicability and precision of exploiting the HFDM and the GFDM to tackle the time-dependent MSE were confirmed, the proposed numerical scheme still needs to be further improved. Hence, our future objective is to extend the present scheme to a nonlinear time-dependent MSE by considering the nonlinear effects to broaden the application range of the model to practical engineering.

Acknowledgements

The authors gratefully acknowledge the National Natural Science Foundation of China (Grant Nos. 51679042 and 52079032) for the financial support of this research.

Publisher's Note Springer Nature remains neutral with regard to jurisdictional claims in published maps and institutional affiliations.

REFERENCES

- Alvarez, A. C., Garcia, G. C., & Sarkis, M. (2017). The ultra weak variational formulation for the modified mild-slope equation. *Applied Mathematical Modelling*, 52, 28–41.
- Álvarez, H. J. C., Fachinotti, V. D., Sarache, P. A. J., Bencomo, A. D., & Puchi, C. E. S. (2018). Implementation of standard penalty procedures for the solution of incompressible Navier-Stokes equations, employing the element-free Galerkin method. *Engineering Analysis with Boundary Elements*, 96, 36–54.
- Battjes, J. (1978). Energy loss and set-up due to breaking random waves. *Proceedings International Conference of Coastal Engineering, New York*, 1(16), 569–587.
- Beels, C., Troch, P., Backer, G. D., Vantorre, M., & Rouck, J. D. (2010a). Numerical implementation and sensitivity analysis of a wave energy converter in a time dependent mild-slope equation model. *Coastal Engineering*, 57(5), 471–492.
- Beels, C., Troch, P., Visch, K. D., Kofoed, J. P., & Backer, G. D. (2010b). Application of the time-dependent mild-slope equations for the simulation of wake effects in the lee of a farm of Wave Dragon wave energy converters. *Renewable Energy*, 35(8), 1644–1661.
- Beji, S., & Nadaoka, K. (1997). A time-dependent nonlinear mild slope equation for water waves. *Proceedings of the Royal Society of London A: Mathematical, Physical and Engineering Sciences*, 453, 319–332.
- Belytschko, T., Krongauz, Y., Organ, D., Fleming, M., & Krysl, P. (1996). Meshless methods: An overview and recent developments. *Computer Methods in Applied Mechanics and Engineering*, 139(1–4), 3–47.
- Benito, J. J., Ureña, F., & Gavete, L. (2001). Influence of several factors in the generalized finite difference method. *Applied Mathematical Modelling*, 25, 1039–1053.
- Berkhoff, J.C.W. (1972). Computation of combined refraction-diffraction. In *Proceedings of the 13th international conference on coastal engineering ASCE* (pp. 471–490).
- Berkhoff, J. C. W., Booy, N., & Radder, A. C. (1982). Verification of numerical wave propagation models for simple harmonic linear water waves. *Coastal Engineering*, 6(3), 255–279.
- Booij, N. (1981). A note on the accuracy of the mild-slope equation. *Report No.81-1, Delft University of Technology, Department. Civil Engineering*.
- Boudjaj, L., Naji, A., & Ghafrani, F. (2019). Solving biharmonic equation as an optimal control problem using localized radial basis functions collocation method. *Engineering Analysis with Boundary Elements*, 107, 208–217.
- Cerrato, A., Rodriguez-Tembleque, L., Gonzalez, J. A., & Aliabadi, M. H. F. (2017). A coupled finite and boundary spectral element method for linear water-wave propagation problems. *Applied Mathematical Modelling*, 48, 1–20.
- Chawla A., Kirby J.T. (1996). Wave transformation over a submerged shoal. CACR Rep. No. 96–03, Dept. of Civ Engrg, University of Delaware, Newark.
- Chen, Q., & Kirby, J. T. (2000). Boussinesq modeling of wave transformation, breaking, and runup. II:2D. *Journal of Waterway Port Coastal & Ocean Engineering*, 126(1), 48–56.
- Dally, W. R., Dean, R. G., & Dalrymple, R. A. (1985). Wave height variation across beaches of arbitrary profile. *Journal of Geophysical Research*, 90(C6), 11917–11927.

- Dean, R. G., & Dalrymple, R. A. (1991). *Water wave mechanics for engineers and scientists*. World Scientific.
- Engquist, B., & Majda, A. (1977). Absorbing boundary conditions for the numerical simulation of waves. *Mathematics of Computation*, 31(139), 629–651.
- Fan, C. M., Chan, H. F., Kuo, C. L., & Yeih, W. (2012). Numerical solutions of boundary detection problems using modified collocation Trefftz method and exponentially convergent scalar homotopy algorithm. *Engineering Analysis with Boundary Elements*, 36, 2–8.
- Fan, C. M., Chua, C. N., Šarler, B., & Li, T. H. (2019). Numerical solutions of waves-current interactions by generalized finite difference method. *Engineering Analysis with Boundary Elements*, 100, 150–163.
- Fan, C. M., Li, H. H., Hsu, C. Y., & Lin, C. H. (2014). Solving inverse Stokes problems by modified collocation Trefftz method. *Journal of Computational and Applied Mathematics*, 268, 68–81.
- Fan, C. M., Li, P. W., & Yeih, W. (2015). Generalized finite difference method for solving two-dimensional inverse Cauchy problems. *Inverse Problems in Science and Engineering*, 23, 737–759.
- Gavette, L., Gavete, M. L., & Benito, J. J. (2003). Improvements of generalized finite difference method and comparison with other meshless method. *Applied Mathematical Modelling*, 27, 831–847.
- Hamidi, M. E., Hashemi, M. R., Talebbeydokhti, N., & Neill, S. P. (2012). Numerical modelling of the mild slope equation using localised differential quadrature method. *Ocean Engineering*, 47, 88–103.
- Härdi, S., Schreiner, M., & Janoske, U. (2019). Enhancing smoothed particle hydrodynamics for shallow water equations on small scales by using the finite particle method. *Computer Methods in Applied Mechanics and Engineering*, 344, 360–375.
- Houbolt, J. C. (1950). A recurrence matrix solution for the dynamic response of elastic aircraft. *Journal of the Aeronautical Sciences*, 17(9), 540–550.
- James, T. (1986). Kirby. A general wave equation for waves over rippled beds. *Journal of Fluid Mechanics*, 162(1), 171–186.
- Karperaki, A. E., Papathanasiou, T. K., & Belibassakis, K. A. (2019). An optimized, parameter-free PML-FEM for wave scattering problems in the ocean and coastal environment. *Ocean Engineering*, 179, 307–324.
- Khellaf, M. C., & Bouhadeif, M. (2004). Modified mild slope equation and open boundary conditions. *Ocean Engineering*, 31(13), 1713–1723.
- Kim, G., Lee, C., & Suh, K. D. (2006). Generation of random waves in time-dependent extended mild-slope equations using a source function method. *Ocean Engineering*, 33(14–15), 2047–2066.
- Kirby, J. T. (1984). A note on linear surface wave-current interaction over slowly varying topography. *Journal of Geophysical Research Oceans*, 89(C1), 745–747.
- Kirby, J. T., & Dalrymple, R. A. (1984). Verification of a parabolic equation for propagation of weakly nonlinear waves. *Coastal Engineering*, 8(3), 219–232.
- Lee, C., & Suh, K. D. (1998). Internal generation of waves for time-dependent mild slope equations. *Coastal Engineering*, 34(1–2), 35–57.
- Lee, C., & Yoon, S. B. (2004). Effect of higher-order bottom variation terms on the refraction of water waves in the extended mild-slope equations. *Ocean Engineering*, 31(7), 865–882.
- Li, J., Feng, X., & He, Y. (2019b). RBF-based meshless local Petrov Galerkin method for the multi-dimensional convection-diffusion-reaction equation. *Engineering Analysis with Boundary Elements*, 98, 46–53.
- Li, P. W., & Fan, C. M. (2017). Generalized finite difference method for two-dimensional shallow water equations. *Engineering Analysis with Boundary Elements*, 80, 58–71.
- Li, Z. C., Wei, Y. M., Chen, Y. K., & Huang, H. T. (2019a). The method of fundamental solutions for the Helmholtz equation. *Applied Numerical Mathematics*, 135, 510–536.
- Lin, J., Chen, W., & Chen, C. S. (2014). A new scheme for the solution of reaction diffusion and wave propagation problems. *Applied Mathematical Modelling*, 38(23), 5651–5664.
- Lin, P. (2004). A compact numerical algorithm for solving the time-dependent mild slope equation. *International Journal for Numerical Methods in Fluids*, 45(6), 625–642.
- Liu, P.L.-F. (1983). Wave-current interactions on a slowly varying topography. *Journal of Geophysical Research Oceans*, 88(C7), 4421–4426.
- Massel, S. R. (1992). *Inclusion of wave-breaking mechanism in a modified mild-slope model, no 1* (Vol. 34, pp. 49–65). Springer.
- Najarzadeh, L., Movahedian, B., & Azhari, M. (2019). Numerical solution of scalar wave equation by the modified radial integration boundary element method. *Engineering Analysis with Boundary Elements*, 105, 267–278.
- Panchang, V. G., Pearce, B. R., Wei, G., & Cushman-Roisin, B. (1991). Solution of the mild-slope wave problem by iteration. *Applied Ocean Research*, 13(4), 187–199.
- Smith, R., & Sprinks, T. (1975). Scattering of surface waves by a conical island. *Journal of Fluid Mechanics*, 72(2), 373–384.
- Song, Z.Y., Zhang, H.G., Kong, J., Li, R.J., Zhang, W. (2007). An efficient numerical model of hyperbolic mild-slope equation. In *Proceedings of the 26th International Conference on Offshore Mechanics and Arctic Engineering* (pp. 253–258).
- Soroushian, A., & Farjoodi, J. (2008). A unified starting procedure for the Houbolt method. *Communications in Numerical Methods in Engineering*, 24(1), 13.
- Tang, J., Shen, Y., Zheng, Y., & Qiu, D. (2004). An efficient and flexible computational model for solving the mild slope equation. *Coastal Engineering*, 51(2), 143–154.
- Tong, F. F., Shen, Y. M., Tang, J., & Cui, L. (2010). Water wave simulation in curvilinear coordinates using a time-dependent mild slope equation. *Journal of Hydrodynamics*, 22(6), 796–803.
- Tsai, C. P., Chen, H. B., & Hsu, J. R. C. (2014). Second-order time-dependent mild-slope equation for wave transformation. *Mathematical Problems in Engineering*, 4, 1–15.
- Ureña, F., Gavete, L., García, A., Benito, J. J., & Vargas, A. M. (2019). Solving second order non-linear parabolic PDEs using generalized finite difference method (GFD). *Journal of Computational and Applied Mathematics*, 354, 221–241.
- Ureña, F., Gavete, L., García, A., Benito, J. J., & Vargas, A. M. (2020). Solving second order non-linear hyperbolic PDEs using generalized finite difference method (GFD). *Journal of Computational and Applied Mathematics*, 363, 1–21.
- Ureña, F., Saleté, E., Benito, J. J., & Gavete, L. (2012). Solving third-and fourth-order partial differential equations using GFD: Application to solve problems of plates. *International Journal of Computer Mathematics*, 89, 366–376.
- Vasarmidis, P., Stratigaki, V., & Troch, P. (2019). Accurate and fast generation of irregular short crested waves by using periodic boundaries in a mild-slope wave model. *Energies*, 12(5), 1–23.

- Wang, L., Wang, Z., & Qian, Z. (2017). A meshfree method for inverse wave propagation using collocation and radial basis functions. *Computer Methods in Applied Mechanics and Engineering*, 322(7), 311–350.
- Young, D. L., Gu, M. H., & Fan, C. M. (2008). The time-marching method of fundamental solutions for wave equations. *Engineering Analysis with Boundary Elements*, 33(12), 1411–1425.
- Zhang, H. S., Zhao, H. J., & Shi, Z. (2007). A finite-difference approach to the time-dependent mild-slope equation. *China Ocean Engineering*, 21(1), 65–76.
- Zhang, T., Huang, Y. J., Liang, L., Fan, C. M., & Li, P. W. (2018). Numerical solutions of mild slope equation by generalized finite difference method. *Engineering Analysis with Boundary Elements*, 88, 1–13.
- Zhang, T., Ren, Y. F., Fan, C. M., & Li, P. W. (2016a). Simulation of two-dimensional sloshing phenomenon by generalized finite difference method. *Engineering Analysis with Boundary Elements*, 63, 82–91.
- Zhang, T., Ren, Y. F., Yang, Z. Q., & Fan, C. M. (2016b). Application of generalized finite difference method to propagation of nonlinear water waves in numerical wave flume. *Ocean Engineering*, 123, 278–290.
- Zhang, Y., Li, Y., & Teng, B. (1995). The new form of time-dependent mild slope equation for random waves, China. *Ocean Engineering*, 9(4), 387–394.
- Zou, Z. L., Jin, H., Zhang, L., et al. (2017). Horizontal 2D fully dispersive nonlinear mild slope equations. *Ocean Engineering*, 129(Jan. 1), 581–604.

(Received August 29, 2020, revised September 14, 2021, accepted September 16, 2021, Published online October 12, 2021)